Synthesis and characterization of Fe-Ti-Sb intermetallic compounds: Discovery of a new Slater-Pauling phase

N. Naghibolashrafi,[1,2,*] S. Keshavarz,[2,3] Vinay I. Hegde,[4] A. Gupta,[2,5,6] W. H. Butler,[2,3] J. Romero,[2,3] K. Munira,[2,3] P. LeClair,[2,3] D. Mazumdar,[7] J. Ma,[8] A. W. Ghosh,[8] and C. Wolverton[4]

[1]*Tri-campus materials science program, The University of Alabama, Tuscaloosa, Alabama 35487, USA*
[2]*Center for Materials for Information Technology, The University of Alabama, Tuscaloosa, Alabama 35487, USA*
[3]*Department of Physics and Astronomy, The University of Alabama, Tuscaloosa, Alabama 35487, USA*
[4]*Department of Materials Science and Engineering, Northwestern University, Evanston, Illinois 60208, USA*
[5]*Department of Chemistry, The University of Alabama, Tuscaloosa, Alabama 35487, USA*
[6]*Department of Chemical and Biological Engineering, The University of Alabama, Tuscaloosa, Alabama 35487, USA*
[7]*Department of Physics, Southern Illinois University, Carbondale, Illinois 62901, USA*
[8]*Department of Electrical and Computer Engineering, University of Virginia, Charlottesville, Virginia 22904, USA*

(Received 10 October 2015; revised manuscript received 30 January 2016; published 29 March 2016)

Compounds of Fe, Ti, and Sb were prepared using arc melting and vacuum annealing. Fe_2TiSb, expected to be a full Heusler compound crystallizing in the $L2_1$ structure, was shown by XRD and SEM analyses to be composed of weakly magnetic grains of nominal composition $Fe_{1.5}TiSb$ with iron-rich precipitates in the grain boundaries. FeTiSb, a composition consistent with the formation of a half-Heusler compound, also decomposed into $Fe_{1.5}TiSb$ grains with Ti-Sb rich precipitates and was weakly magnetic. The dominant $Fe_{1.5}TiSb$ phase appears to crystallize in a defective $L2_1$-like structure with iron vacancies. Based on this finding, a first-principles DFT-based binary cluster expansion of Fe and vacancies on the Fe sublattice of the $L2_1$ structure was performed. Using the cluster expansion, we computationally scanned $>10^3$ configurations and predict a novel, stable, nonmagnetic semiconductor phase to be the zero-temperature ground state. This new structure is an ordered arrangement of Fe and vacancies, belonging to the space group $R3m$, with composition $Fe_{1.5}TiSb$, i.e., between the full- and half-Heusler compositions. This phase can be visualized as alternate layers of $L2_1$ phase Fe_2TiSb and $C1_b$ phase FeTiSb, with layering along the [111] direction of the original cubic phases. Our experimental results on annealed samples support this predicted ground-state composition, but further work is required to confirm that the $R3m$ structure is the ground state.

DOI: 10.1103/PhysRevB.93.104424

I. INTRODUCTION

The ternary intermetallic Heusler compounds with compositions X_2YZ ("full" Heusler) and XYZ ("half" Heusler) have been a subject of great interest in spintronics owing to the fact that many of them are predicted to be "half-metallic" ferromagnets [1]. The term "half-metallic" refers to the existence of a gap in the density of states at the Fermi level for one spin channel and not for the other, leading to the possibility of 100% spin polarization of the electron current. Additionally, many of these Heusler compounds have relatively high Curie temperatures, raising the possibility of high polarization at or above room temperature [1–5].

We recently completed a first-principles study of over 500 candidate full- and half-Heusler compounds, with a view to identify unstudied materials that were predicted to be stable and half-metallic. After screening candidate materials identified by the first-principles study from an experimental point of view (e.g., toxicity, fabricability, homogeneity, possibility of decomposition into more stable binary compounds, etc.) and examining the available literature, we found a number of promising candidate materials [6,7]. One of the most intriguing was Fe_2TiSb, which was predicted by the calculations to have a negative formation energy and to be a (near) half-metal in the $L2_1$ structure. Perhaps surprisingly, a literature survey found no reports of the magnetic and spintronic properties of this or related compounds. This made an inquiry into this metallurgical system potentially interesting, particularly as a test case for our methods of identifying new compounds. The study reported here examines the possibility of synthesizing Fe_2TiSb and related compounds in a pure phase form, and a consequent analysis of their structural and magnetic properties. One of the interesting insights of our study based on a combination of theory and experiment is that Fe_2TiSb may prefer to form as a naturally layered Heusler compound with layers of the full Heusler, Fe_2TiSb, alternating with layers of the half-Heusler, FeTiSb. The predicted lowest energy phase with composition $Fe_{1.5}TiSb$ is a nonmagnetic semiconductor, consistent with experimental observations.

II. ELECTRONIC STRUCTURE OF STOICHIOMETRIC HEUSLER COMPOUNDS BASED ON FE, TI, AND SB

A. Full Heusler

Our first-principles survey included 180 prospective full-Heusler compounds in the $L2_1$ structure (composition X_2YZ) and 378 prospective half-Heusler compounds in the $C1_b$ structure (composition XYZ). The full results of this study and the details on the methods and parameters of the calculations are available on a website [8]. Among the potentially interesting systems that emerged from these studies are compounds of Fe, Ti, and Sb. Considering first the hypothetical Fe_2TiSb

*nnaghibolashrafi@crimson.ua.edu

compound in the $L2_1$ structure, we found it to be stable against decomposition into its constituent elements with an energy of formation of -0.264 eV/atom and a lattice constant of $a = 0.604$ nm. We also found it to be stable with respect to tetragonal distortion. The most stable magnetic configuration for this phase (considering ferromagnetic, ferrimagnetic, antiferromagnetic, and nonmagnetic configurations) is a ferrimagnetic ground state with saturation magnetization of approximately $1.00\mu_B$ per formula unit at $T = 0$ K. The magnetization is primarily on the Fe sites ($0.69\mu_B$) but with a significant opposite ($-0.31\mu_B$) moment on the Ti and a small ($-0.03\mu_B$) moment on the Sb. The quoted moments are those within spheres of radius 0.145nm centered on each atom. The value of the calculated total moment ($\sim 1.00\mu_B$) causes one to suspect that this solution to the DFT equations is a "Slater-Pauling phase."

We use the term "Slater-Pauling phase" to describe full and half-Heusler compounds that satisfy a generalization [9–11] of the rule first enunciated by Slater and Pauling [12–14], which states that compounds based on the bcc crystal structure tend to have three electrons per atom in the minority-spin channel. For the Heusler half-metals, the generalization of the Slater-Pauling rule is that there tends to be a gap in the density of states for one of the spin-channels with precisely three valence electron states per atom in the gapped channel below the gap. When there is a gap like this and when the Fermi energy falls in the gap, we will refer to the phase as a Slater-Pauling half-metal. Often, there is a gap with three electrons per atom, but the Fermi energy falls just above or just below the gap. We refer to such phases as "Slater-Pauling near half-metals." Following this terminology, our DFT calculations predict $L2_1$ Fe_2TiSb to be a Slater-Pauling near half-metal. It has a gap in the minority spin channel of 0.31 eV, as shown in Fig. 1. The Fermi energy falls just below (0.05 eV) the edge of the gap so that the number of minority electrons is calculated to be 11.99915 rather than 12. Since the total number of electrons per formula unit is 25, there must be 13.00085 majority spin electrons yielding a moment of 1.0017 μ_B per formula unit. A moment of exactly 1.0 μ_B would have produced a Slater-Pauling half-metal.

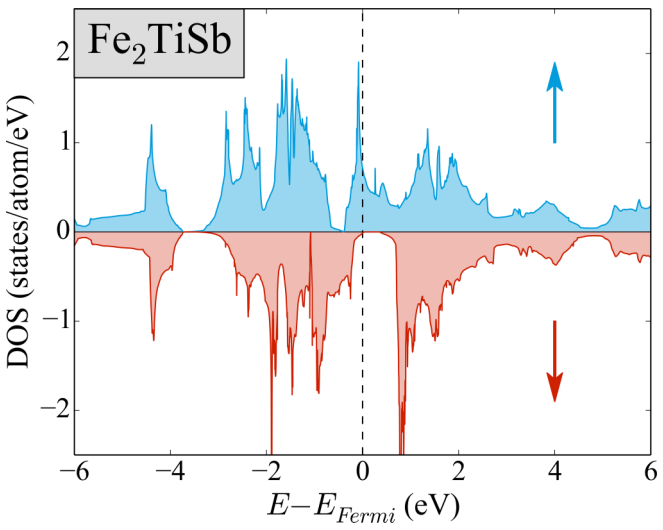

FIG. 1. Calculated density of states for $L2_1$ Fe_2TiSb.

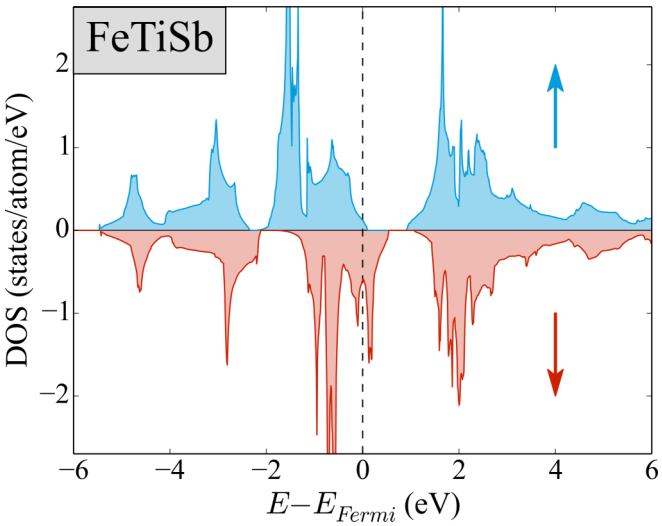

FIG. 2. Calculated density of states for $C1_b$ FeTiSb.

B. Half-Heusler

Subsequent to our survey of full-Heusler compounds, we completed a survey of the half-Heusler ($C1_b$) compounds. We found that $C1_b$ phase FeTiSb is also predicted to be stable relative to decomposition into its constituent elements and tetragonal distortions of its cell, with an energy of formation of -0.382 eV/atom and a lattice constant of 0.595 nm. The density of states of FeTiSb is shown in Fig. 2. The lowest-energy magnetic configuration is predicted to be a Slater-Pauling near half-metal with a magnetic moment of approximately $1\mu_B$ per formula unit. FeTiSb actually has Slater-Pauling gaps in both spin channels. One, however, is quite close to the Fermi energy. The calculated Fermi energy is 0.11 eV below the gap in the majority channel, so that only 8.9775 states are occupied rather than the nine that would have been occupied had the Fermi energy fallen in the majority gap. FeTiSb has 17 valence electrons, so subtracting the 8.9775 majority electrons yields 8.0225 minority electrons for a predicted moment per formula unit of 0.955 μ_B. This system is also predicted to be ferrimagnetic with moments of $1.3\mu_B$ on the Fe and $-0.35\mu_B$ on the Ti. Half-heuslers typically have larger gaps than full-Heuslers. The calculated width of the Slater-Pauling gap is 0.85 eV.

III. EXPERIMENTAL

Based on the initial theoretical findings, we attempted to synthesize bulk samples of both the full Heusler Fe_2TiSb and the half-Heusler FeTiSb. Stoichiometric ratios of pure elements Fe (Alfa Aesar, 99.98%), Ti (Alfa Aesar, 99.9%), and Sb (Alfa Aesar, 99.999%) were mixed together and melted using an Edmund Buehler Mini MAM-1 compact arc melting system under an ultrahigh purity Argon (99.999%) pressure of 0.02 Pa. A 10% excess of Sb was added to the initial melt to compensate for losses in the final ingot due to its higher volatility. A small piece of Ti was melted before all arc melting runs as an oxygen getter to avoid oxidization of the sample. Ingots were remelted at least five times to ensure the homogeneity of the material.

The samples from the arc-melter were cut and mounted for metallographic studies. A JEOL 7000 Field emission scanning electron microscope (SEM) was used for energy-dispersive x-ray spectroscopy (EDS) analysis to ensure that the chemical composition of the as-cast ingots had not deviated from the intended target stoichiometry. Samples for heat treatment were wrapped in Ta foil and sealed under vacuum in quartz tubes to avoid oxidation. These pieces were heat treated at various temperatures (400–1100°C) and dwell times (1–15 days). From metallographic and x-ray diffraction analysis of the annealed samples, a treatment at 900 °C for 7 days and cooled in the furnace at approximately 70 degrees per hour appeared to result in the optimum $L2_1$ structure and granular microstructure for all cases.

The crystal structures of the annealed samples were studied using a Bruker D8 Discover X-Ray Diffraction (XRD) system with a monochromatic Co K_α radiation. In order to minimize surface effects, the samples were mounted and polished, and rotated around the φ axis during the XRD measurement. Electron backscatter diffraction (EBSD) phase mapping using the JEOL 7000 FE-SEM system was additionally performed to affirm the structure determined from XRD. Simulated XRD patterns were obtained both by using the CARINE crystallography 4.0 software as well as by direct calculation to account for dispersive corrections to the atomic scattering factors [15,16], while the Rietveld refinement was carried out using the CRYSTAL IMPACT MATCH! software based on the FULLPROF algorithm [17]. The magnetic properties were measured using Quantum Design Physical Property Measurement System (PPMS) Dynacool with vibrating sample magnetometry (VSM) feature.

IV. EXPERIMENTAL RESULTS

A. Fe_2TiSb

All of the as-cast Fe_2TiSb samples heat-treated at 900 °C for soaking times of 3, 5, 7, or 9 days showed a single, mostly granular microstructure. Energy-dispersive x-ray spectroscopy showed the composition of the grains to be $Fe_{40}Ti_{30}Sb_{30}$, with an uncertainty of ∼5% in the abundance of each element, and thus quite significantly different from the intended stoichiometry—in spite of the fact that the as-cast samples were essentially stoichiometric Fe_2TiSb. Henceforth, we will refer to this nominal composition as $Fe_{1.5}TiSb$ for simplicity. Figure 3 shows an example of such microstructure and its relevant EDS result for a sample heat treated at 900°C for 7 days. X-ray diffraction results on these samples, discussed further below, were consistent with a $L2_1$ phase alongside a small amount of an Fe-rich precipitate phase.

Since the stoichiometry of the grains deviated significantly from the initial as-cast composition of Fe_2TiSb, we hypothesized that the bulk of the material was crystallized in the form of $Fe_{1.5}TiSb$ grains, while the remaining iron precipitated in the grain boundaries and disappeared at the etching stage (used to prepare the specimens for metallographic imaging). In order to test this hypothesis, we performed an EDS analysis of nonetched samples, and indeed found an overall composition of Fe_2TiSb, consistent with the as-cast material and indicating a loss of iron after metallographic etching. X-ray diffraction

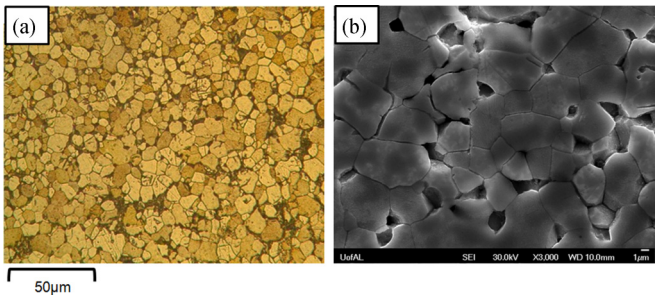

FIG. 3. (a) The metallography image of an Fe_2TiSb sample heat treated at 900 °C for 7 days. The sample was etched for 30 seconds using the marble etchant. The microstructure is evidently single grain, while the voids can be attributed to an Fe-rich precipitate at the grain boundaries, which was removed by the marble etchant. (b) SEM micrograph of the same surface showing the grain structure. EDS indicated that the composition of the grains was $Fe_{40}Ti_{30}Sb_{30}$.

analysis of the pre-etched material also indicates the presence of peaks corresponding to an iron-rich $Fe_{0.975}Ti_{0.025}$ bcc solid-solution in addition to the full-Heusler $L2_1$ phase peaks originating from the $Fe_{1.5}TiSb$ grains. The etched sample, on the other hand, showed only a very small (∼1%–2%) presence of the iron rich phase.

Figure 4(a) shows the XRD patterns of *etched and polished* samples measured with Co K_α radiation. The XRD patterns generated by either CARINE 4.0 simulations or CRYSTAL IMPACT MATCH are similar to the pattern observed. Rietveld refinement gives good agreement ($\chi^2 = 0.9$ and average $R_{\text{Bragg}} = 0.1$) between the data and the calculated pattern for the $L2_1$ structure of the dominant phase with the experimental lattice constant of 0.5967 nm. One can also clearly see small peaks corresponding to an Fe-rich phase identified as $Fe_{0.975}Ti_{0.025}$ (e.g., at approximately ∼52°), which are much clearer in the pre-etched samples. For the pre-etched sample, we estimate from Rietveld refinement and EBSD that the Fe-rich phase constitutes about ∼10% of the total, and approximately the same amount of bcc Fe for the etched samples was estimated from magnetometry (see below).

The presence of all low-angle $L2_1$ peaks, i.e., (111), (200), and (220) effectively rules out the possibility of significant deviation toward a B2 or A2 disorder. If the (111) peak were missing or reduced, this would have indicated Ti-Sb mixing and generated a B2 structure, whereas a missing or reduced (200) peak would have indicated Fe-(Ti,Sb) mixing and generated the A2 (bcc) structure [18–20]. In fact, the (111) and (200) superstructure peaks are somewhat higher in intensity than expected compared to the (220) fundamental peak. The higher than expected values of intensities of the superlattice peaks could be attributed to surface effects and texture, or they could be indicative of the fact that the $Fe_{1.5}TiSb$ grains are not stoichiometric for a $L2_1$ structure. If we presume for the moment that we do not have a preferred texture in our samples, the trend of the x-ray diffraction intensities with Fe content can be readily seen. If we consider an Fe_2TiSb compound in the $L2_1$ structure, with Fe at the 8c ($\frac{1}{4}$, $\frac{1}{4}$, $\frac{1}{4}$) Wyckoff positions, the structure factors for the main peaks of

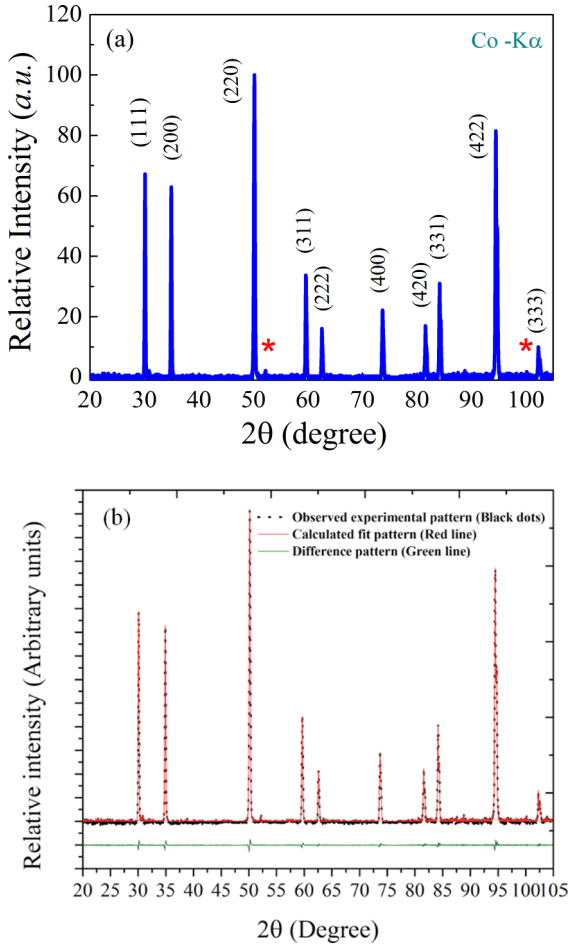

FIG. 4. (a) The XRD pattern measured using Co K_α radiation of the Fe_2TiSb sample heat treated at 900 °C for 7 days. The pattern is consistent with an $L2_1$ structure with a lattice parameter of 0.5957 nm for the $Fe_{1.5}TiSb$ grains. The stars indicate peaks attributed to an Fe-rich precipitate. (b) The lattice value is also confirmed by a Rietveld refinement analysis with good agreement with the proposed model.

interest are [18–20]

$$F_{111} = 4|f_{\mathrm{Ti}} - f_{\mathrm{Sb}}|, \tag{1}$$

$$F_{200} = 4|f_{\mathrm{Ti}} + f_{\mathrm{Sb}} - 2f_{\mathrm{Fe}}|, \tag{2}$$

$$F_{220} = 4|f_{\mathrm{Ti}} + f_{\mathrm{Sb}} + 2f_{\mathrm{Fe}}|, \tag{3}$$

where f_i is the total atomic scattering factor for element i. From this we can see that having less Fe than expected would reduce the (220) x-ray structure factor and increase the (200) structure factor (leaving the (111) structure factor unchanged), consistent with the XRD results. A more quantitative analysis, including the dispersive terms in the atomic scattering factors [15,16], does give a 111/200 intensity ratio similar to that observed using a nominal Fe content of 1.4–1.6 rather than 2.0. However, we stress that we cannot rule out a net preferred texture in our samples that would alter the relative XRD intensities. Indeed, this is likely the case given that the (220) peak intensity is still smaller than expected compared to the (111) and (200) peaks. Still, with the *assumption* that we have

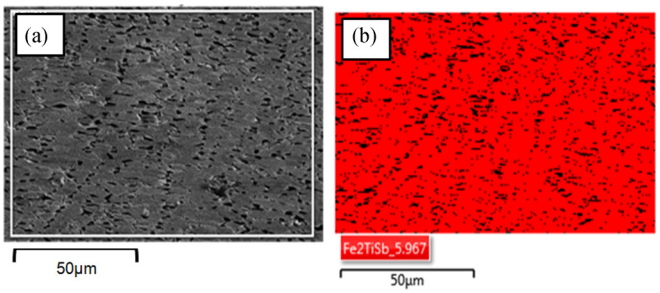

FIG. 5. (a) The electron micrograph of the as-cast Fe_2TiSb sample heat treated at 900 °C for 7 days taken by EBSD (b) the phase colormap scan shows 90% (red color) of the sample has a homogenous $L2_1$ structure with a lattice constant of 0.5967 nm.

no preferred texture, both qualitatively and quantitatively the XRD intensities do appear to be consistent with an Fe-deficient $L2_1$ $Fe_{1.5}TiSb$ compound.

In order to further substantiate the existence of the $L2_1$ structure, an EBSD phase map was performed. The phase mapping showing the $L2_1$ structure is shown in Fig. 5. More than 90% of the microstructure is colored red which means that the material corresponding to an $L2_1$ phase with a lattice constant of 0.5967 nm is homogenous throughout the sample. This is further evidence that the grains are crystallizing in a cubic $L2_1$ structure. The remaining 10% of the sample is attributed to the Fe-rich phase precipitated at the grain boundaries, which are not evident in the EBSD maps. The fact that the dominant phase has a composition of approximately $Fe_{1.5}TiSb$ rather than Fe_2TiSb expected for an ideal $L2_1$ compound points toward possible Fe vacancies.

Magnetic characterization of the as-cast Fe_2TiSb sample heat treated for 7 days at 900 °C shows the sample has a ferromagnetic component with a small hysteresis, which does not completely saturate for the magnetic fields of up to 7200 kA/m (9 T) at 5 K, Fig. 6(a). This behavior is suggestive of small ferromagnetic Fe-rich precipitates in a weakly paramagnetic matrix. We find the magnetization to be 27 Am^2/kg at the maximum applied field of 7200 kA/m, with a coercivity of 2 kA/m. The ferromagnetic component would correspond to a very low magnetization for the dominant phase, but does agree well with ∼10% of the sample having approximately the same magnetization as bcc Fe (or a very Fe-rich phase). We hypothesize, therefore, that the magnetic behavior comes from a superposition of a small volume fraction (∼10%) of strongly ferromagnetic Fe-rich precipitates at the $Fe_{1.5}TiSb$ grain boundaries, and a large volume fraction of $Fe_{1.5}TiSb$ grains that are weakly paramagnetic. Temperature-dependent magnetization [Fig. 6(b)], measured at an applied(field of $H = 80$ kA/m during heating, is relatively uniform up to 400 K, consistent with most of the Fe-rich precipitate material being strongly ferromagnetic. The exception is a small upturn in the magnetization for temperatures below 10 K, which again could originate from weakly paramagnetic $Fe_{1.5}TiSb$. It would be unusual for a bulk sample to exhibit such a large Curie temperature (apparently above 400 K) with such a small moment (approximately 10% the mass magnetization of Fe). This again suggests that the observed ferromagnetic component comes not from the bulk, but from the Fe-rich

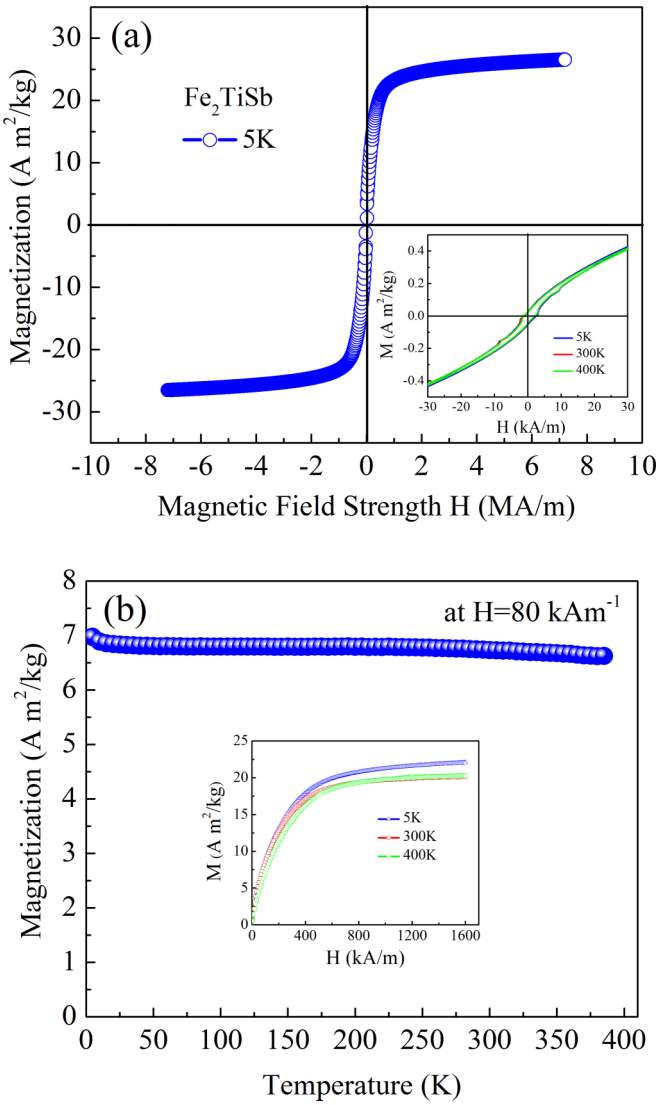

FIG. 6. (a) Magnetization curve of a nominally Fe_2TiSb sample at 5 K shows the dominant ferromagnetic nature of the sample. The inset is the magnetization around the origin, showing the small coercive field from the Fe-rich precipitates. (b) Temperature-dependent magnetization shows no sign of phase transformation or Curie temperature below 400 K. The inset is the magnetization curve at 5, 300, and 400 K showing only a minor change in the magnetization from 5 to 400 K.

(nominally $Fe_{0.975}Ti_{0.025}$ from the observed XRD peaks) precipitate material, from which we would expect a high Curie temperature and low coercivity. Interestingly, first-principles calculations (discussed below in Sec. V) for $Fe_{1.5}TiSb$, close to the observed composition for the dominant phase, indicate that a nonferromagnetic ground state is indeed favored.

B. $Fe_{1.5}TiSb$

Our observations during the synthesis of Fe_2TiSb suggested that $Fe_{1.5}TiSb$ is, in fact, a more stable phase, a result corroborated by first principles calculations discussed in Sec. V. Given this, the $Fe_{1.5}TiSb$ compound seemed worthy of direct synthesis. As-cast samples were prepared in the same fashion as Fe_2TiSb. After the $Fe_{1.5}TiSb$ samples were heat

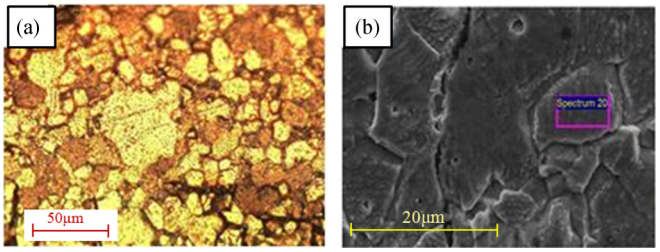

FIG. 7. (a) An optical micrograph of an as-cast $Fe_{1.5}TiSb$ sample heat treated at 900 °C for 7 days. The sample was etched for 30 seconds using marble etchant. The microstructure reveals single grains without the presence of any secondary phase in the grain boundaries. (b) An SEM micrograph of the same surface showing the grain structure. EDS indicated that the composition of the grains was $Fe_{1.44}TiSb_{1.12}$.

treated at 900 °C for 7 days, a single grain microstructure was observed. There were no signs of precipitates. Figure 7 shows optical and SEM micrographs. Energy-dispersive x-ray spectroscopy shows that the grains present in the sample have a nominal stoichiometry of $Fe_{1.44}TiSb_{1.12}$. Again, for simplicity, we will refer to this nominal composition as $Fe_{1.5}TiSb$, and it appears that this particular phase is metallurgically stable in a wide range of iron doping within the $Fe_{1+x}TiSb$ alloy system.

The XRD data, Fig. 8, indicate the presence of a phase in an $L2_1$ structure with a lattice parameter of 0.5967 nm, which is in concordance with our observations for Fe_2TiSb. This shows that there is a possible limit of solubility for iron at the $Fe_{1.5}TiSb$ composition, which is evidently the stable phase, and additional iron will be precipitated in the grain boundaries of the dominant $L2_1$ phase.

To perform further comparison between the diffraction pattern of Fe_2TiSb and $Fe_{1.5}TiSb$ and verify the crystal structure, a selected area electron diffraction (SAED) analysis using a FEI Tecnai F-20 Transmission Electron Microscope (TEM) was performed. Results are shown in Fig. 9. The diffraction of the Fe_2TiSb sample showed patterns belonging to both bcc α-Fe and $L2_1$ phases, which is in accordance with our findings suggesting Fe precipitation in this compound. The

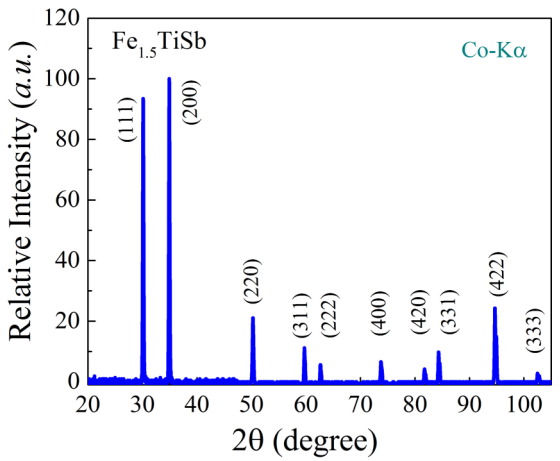

FIG. 8. The XRD pattern measured using Co K_α radiation of the $Fe_{1.5}TiSb$ compound. All peak positions can be attributed to an $L2_1$ structure with a lattice constant of 0.5967 nm.

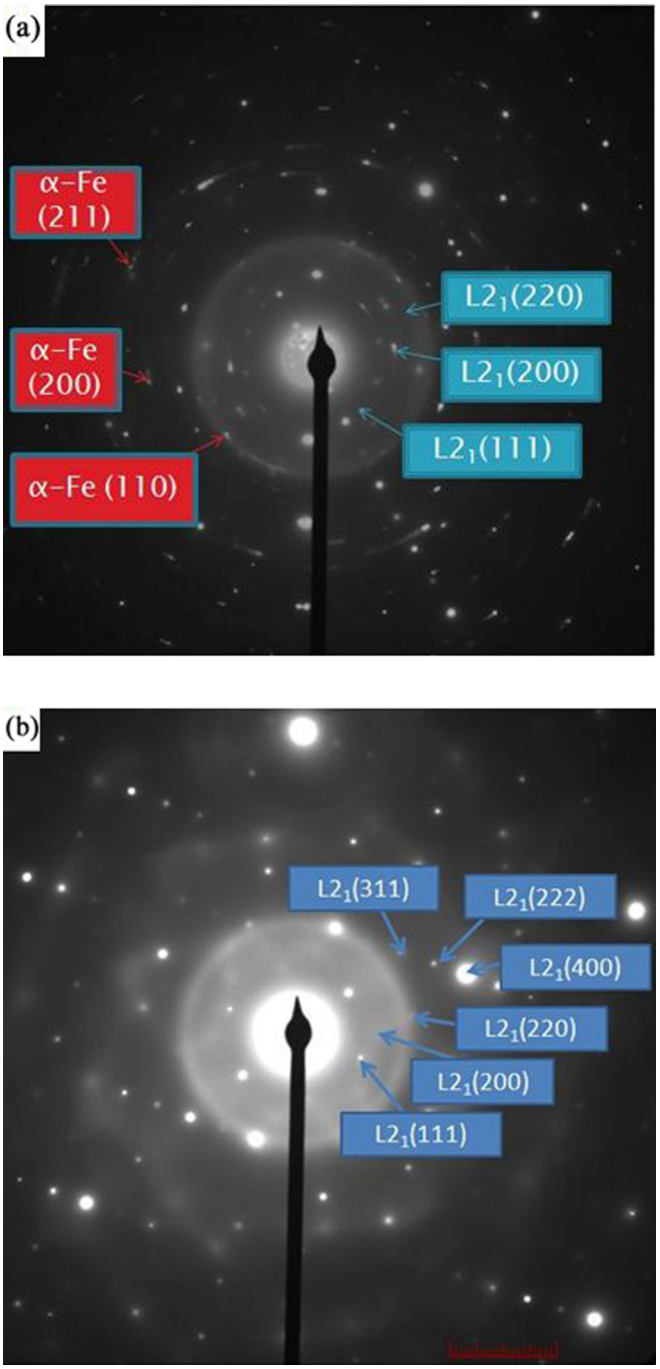

FIG. 9. (a) A SAED ring pattern of Fe_2TiSb sample after heat treatment at 900 °C for 7 days. Both bcc Fe and $L2_1$ patterns are visible. (b) A SAED pattern of $Fe_{1.5}TiSb$ heat treated at 900 °C for 7 days. There are spots visible belonging to the assumed $L2_1$ structure, but none corresponding to bcc Fe.

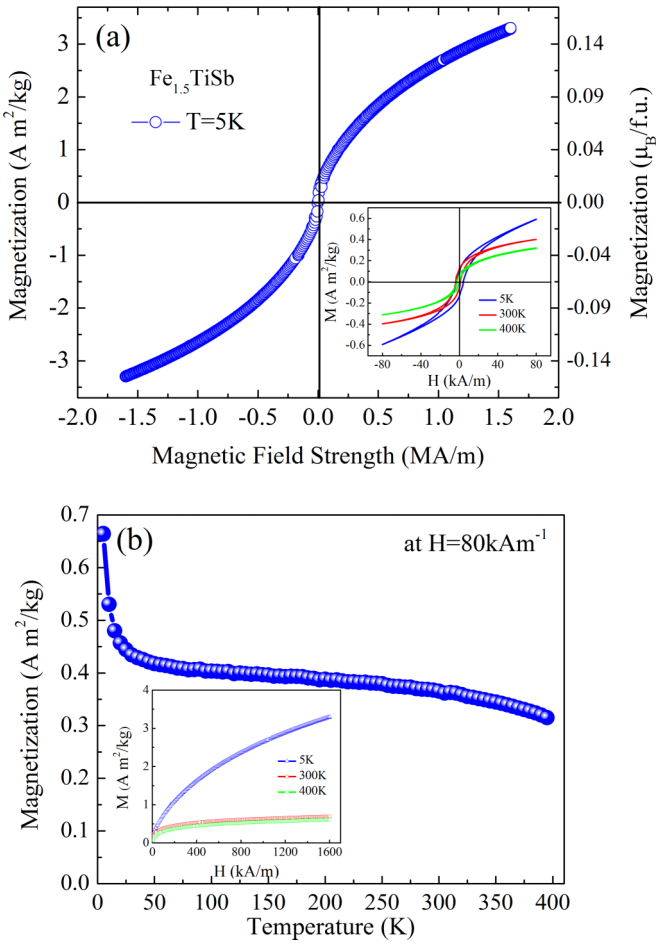

FIG. 10. (a) The magnetization of $Fe_{1.5}TiSb$ shows no indication of saturation for the fields up to 7200 kA/m at $T = 5$ K, showing the paramagnetic nature of the dominant phase. The inset shows small coercivity related to Fe-rich phase precipitates. (b) Magnetization of the sample as a function of temperature measured in an applied field of $H = 80$ kA/m during heating. The inset shows the magnetization curves measured at temperatures 5, 300, and 400 K.

pattern is noticeably different for the $Fe_{1.5}TiSb$ sample—the Fe patterns is no longer present, while the $L2_1$ pattern is still clearly visible. It is notable that the pattern belonging exclusively to the $L2_1$ phase has faded, which could be attributed to the presence of Fe vacancies in the $L2_1$ lattice, which would also be consistent with Fe precipitation.

The magnetic properties of the $Fe_{1.5}TiSb$ material are qualitatively similar to those of the Fe_2TiSb material, with a smaller amount of the Fe-rich phase (∼1.5%). Magnetization versus field characteristics at $T = 5$ K, Fig. 10, again suggests paramagnetic behavior of the dominant $L2_1$ phase plus weak ferromagnetism from the small concentration of Fe-rich grains segregated at the grain boundaries. Coercivity in the low-temperature regime is approximately 2 kA/m for Fe_2TiSb sample, as shown in the inset of Fig. 10(a). Magnetic measurements up to 7200 kA/m for this sample shows no sign of saturation of the magnetization at $T = 5$ K, whereas at $T =$ 300 and 400 K the magnetization is nearly saturated with only 100 kA/m. Figure 10(b) shows the temperature-dependent magnetization, measured in similar conditions as the Fe_2TiSb sample. As in that case, the temperature dependence appears to be a superposition of weak paramagnetism of the dominant $Fe_{1.5}TiSb$ phase and a small ferromagnetic component due to the Fe-rich segregations at the grain boundaries. The magnetization does not change significantly over the whole temperature range, aside from the upturn in temperatures below 10 K. Due to the smaller concentration of Fe-rich precipitates in the $Fe_{1.5}TiSb$ sample (estimated as ∼1.5%),

the maximum magnetization measured is much smaller than for the Fe_2TiSb sample [Fig. 10(b) inset].

C. FeTiSb

Finally, the half-Heusler FeTiSb composition was expected from our theoretical survey to also have a negative energy of formation and to be a near half-metallic compound. As-cast samples of nominal composition FeTiSb were prepared and heat treated in a similar fashion to the previous samples. Microstructural analysis on samples annealed to 900 °C for 7 days shows that the material in fact decomposes into two separate phases. One is again the iron rich $Fe_{1.5}TiSb$ phase, but with a significant presence of a Ti-Sb rich phase. Figure 11 displays optical and SEM micrographs. The composition of the Ti-Sb rich phase was found by EDS to be approximately $Sb_{1.8}Ti_{1.5}Fe$. While once again the dominant phase is $Fe_{1.5}TiSb$, in previous cases it was excess Fe, which segregated to the grain boundaries. In contrast, in this case, excess Ti and Sb have formed a new granular phase, indicating that the level of solubility of the dominant phase for Ti and Sb might be less than its solubility level for Fe. Figure 12 shows XRD pattern of the sample. It clearly indicates the presence of the $L2_1$ phase again, which originates from the $Fe_{1.5}TiSb$ grains, as well as small yet-unidentified peaks at low angles, which are presumably attributable to the Ti-Sb rich grains. The relative peak intensities in this case are probably a reflection of an induced texture in the sample.

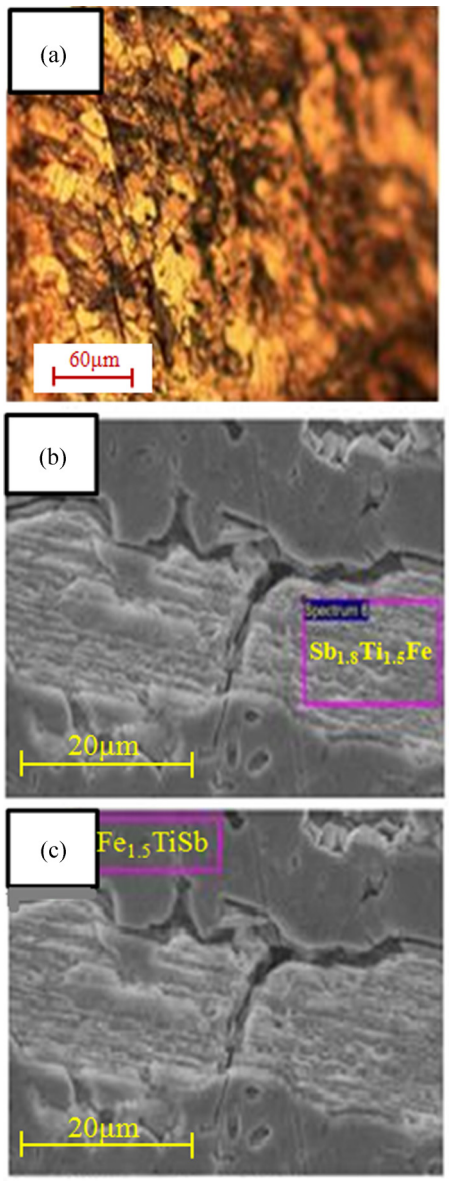

FIG. 11. (a) An optical metallography image of FeTiSb exhibiting two distinct granular phases present. (b) shows the SEM micrograph of an iron poor grain, whose composition was found to be $Sb_{1.8}Ti_{1.5}Fe$. (c) shows an iron-rich grain, whose composition was found to be $Fe_{1.5}TiSb$.

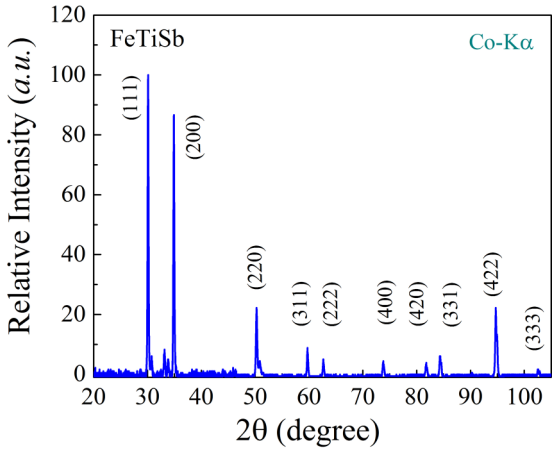

FIG. 12. The XRD pattern measured using Co K_α radiation of the as-cast FeTiSb compound. Most peak positions can be attributed to an $L2_1$ structure while there are some yet-unidentified peaks possibly arising from the Ti-Sb rich phase.

Magnetization versus field of the FeTiSb sample, illustrated in Fig. 13, has a similar behavior to $Fe_{1.5}TiSb$. We again attribute the paramagnetic response to the $Fe_{1.5}TiSb$ phase, but in this case the contribution we attribute to the precipitates is different. Comparing the magnetization results from Fe_xTiSb ($x = 1,1.5,2$) samples, the common presence of the stable and weakly paramagnetic $Fe_{1.5}TiSb$ phase is apparent, with a varying ferromagnetic contribution of Fe-rich precipitates for Fe_2TiSb and $Fe_{1.5}TiSb$ samples and TiSb-rich phase for the case of FeTiSb. Magnetization versus temperature (Fig. 13) gives a similar conclusion: ferromagnetic precipitates give a slowly-varying contribution to the magnetization.

In order to verify the nature of magnetization versus temperature upturn for $T < 10$ K, field-cooling (FC) and zero-field-cooling (ZFC) measurements were performed to check for the presence of superparamagnetism in the samples, which would help determine if observed paramagnetism is indeed due to the dominant $Fe_{1.5}TiSb$ grains or small precipitates. The outcome, shown in Fig. 14, does not show the expected bifurcation for superparamagntic effects for either the Fe_2TiSb or $Fe_{1.5}TiSb$ samples. Therefore the main source of the increased magnetization for $T < 10$ K, as well as the nonsaturated magnetization versus field at low temperatures, is most likely due to weak paramagnetism of the dominant phase $Fe_{1.5}TiSb$.

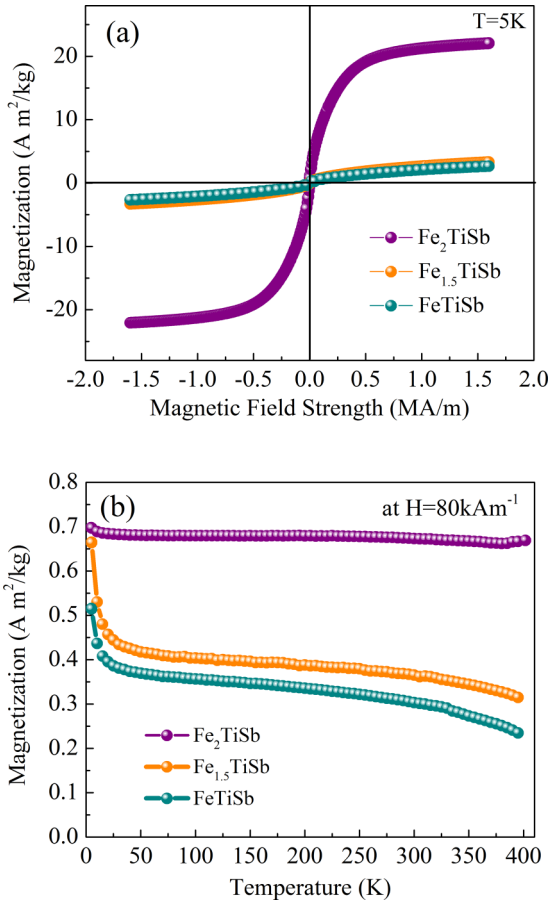

FIG. 13. (a) Magnetization curves for Fe_xTiSb ($x = 1, 1.5, 2$) specimens. (b) Temperature-dependent magnetization of these samples measured in the applied field of $H = 80$ kA/m during the heating.

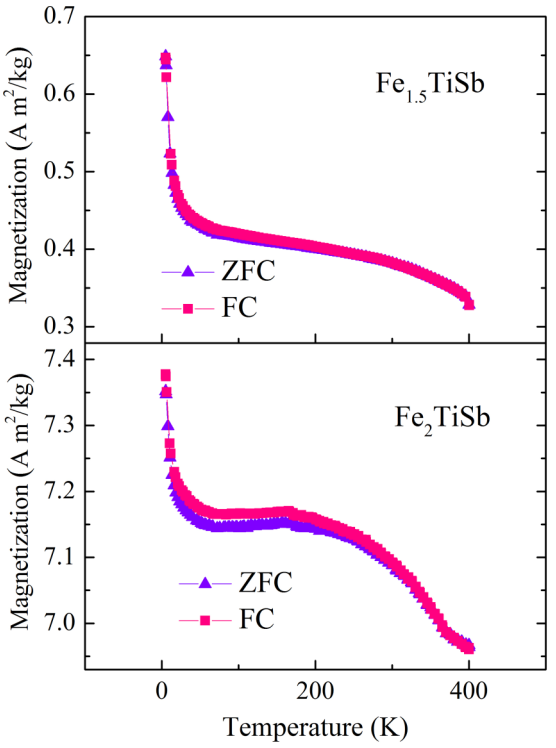

FIG. 14. Field-cooling and zero field cooling of $Fe_{1.5}TiSb$ and Fe_2TiSb samples confirm the absence of superparamagnetism in these samples.

Overall, one concludes at this point that regardless of the starting composition, it is the $Fe_{1.5}TiSb$ phase that is most stable, and it appears to dominate after heat treatment. This phase crystallizes in the $L2_1$ structure, albeit one with iron sites which are approximately 2/3 to 3/4 occupied, and seems to exhibit weak paramagnetism. Starting from an Fe-rich composition leads to segregation of excess Fe to grain boundaries of the $Fe_{1.5}TiSb$ grains, while starting from an Fe-poor composition leads to a secondary Ti-Sb-rich phase appearing. The main question to be addressed from a theoretical point of view is whether the greater stability of the $Fe_{1.5}TiSb$ phase compared to FeTiSb or Fe_2TiSb can be explained, whether its existence in a (defective) $L2_1$ or related structure can be explained, and whether one expects it to be nonmagnetic.

V. CLUSTER EXPANSION: FE-DEFICIENT, HEUSLER-BASED STRUCTURES

The experimental work described in Secs. III and IV makes clear that the lowest energy structure in the Fe-Ti-Sb system is based on the $L2_1$ structure. It is also clear that it is not simply a Fe_2TiSb full-Heusler compound, and specifically, it is Fe deficient. Given this experimental input, we performed a binary cluster expansion (CE) of Fe and vacancies (hereafter, a vacancy is indicated as □) on the Fe sublattice of the Fe_2TiSb $L2_1$ structure in an attempt to explain the predisposition of the Fe-Ti-Sb to tolerate Fe deficiency.

We calculated the formation energy ΔH_f (per mixing site) of a compound with composition $Fe_x\square_{2-x}TiSb$ with respect to the end members Fe_2TiSb and $\square_2TiSb$ using

$$\Delta H_f = \tfrac{1}{2}[E(Fe_x\square_{2-x}TiSb) - x\,E(Fe_2TiSb) - (2-x)E(\square_2TiSb)] \quad (4)$$

where all the required energies are calculated using density functional theory (DFT). The parameters used for all calculations, and other details are discussed in Appendix A. We fit a binary CE to the formation energies calculated using Eq. (4) by minimizing the sum of squares of the residuals. We generated new structures, used their formation energies in the fit, and added terms to the CE until the cross-validation (CV) score was minimized, and adding further structures resulted in overfitting (see Appendix B for further details). We found a well-converged CE, with a CV score of ~ 20 meV/mixing atom by using 66 $Fe_x\square_{2-x}TiSb$ structures and their formation energies in our fit (Fig. 15). We searched for ground states by computationally scanning through $>10^3$ structures, which corresponds to a complete enumeration of all possible Fe/□ orderings with <20 atoms per cell [21]. Out of this extremely large configuration space, we predict a novel, stable ground state phase with a composition $Fe_{1.5}TiSb$, i.e., between the full-Heusler and half-Heusler compositions, belonging to the trigonal $R3m$ space group, and with a formation energy of -0.223 eV/mixing atom. This structure corresponds to a

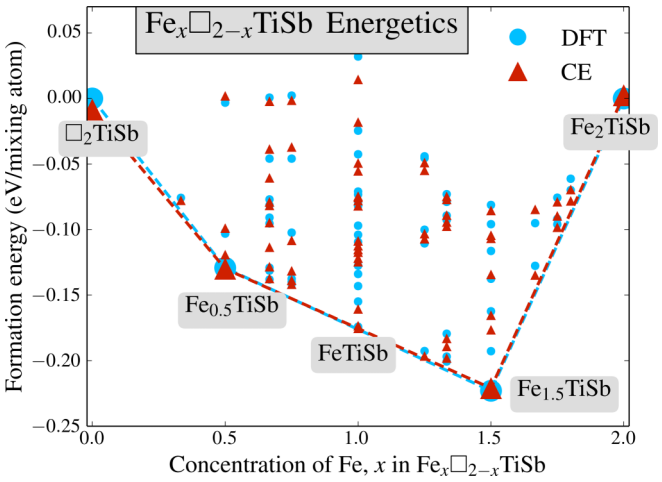

FIG. 15. Energies of 66 different arrangements of Fe and □ on the Fe sublattice of Fe_2TiSb in the $L2_1$ structure, calculated using DFT, and those predicted by a binary cluster expansion (CE) fit to the DFT energies. The DFT convex hull is captured well by the CE, with a cross-validation error of ∼20 meV/mixing atom.

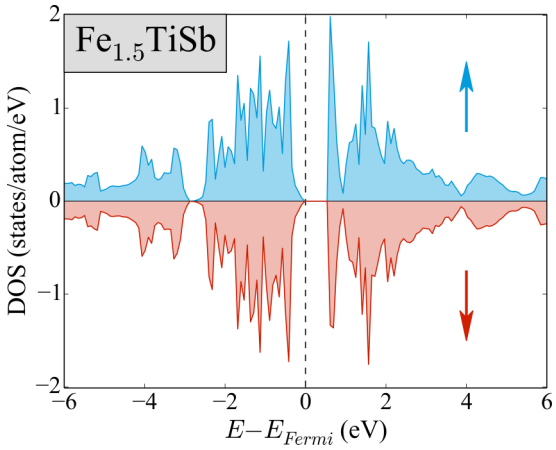

FIG. 17. The density of electronic states of the low-energy $Fe_{1.5}TiSb$ $R3m$ structure predicted by the cluster expansion. It is a nonmagnetic semiconductor with gaps in both the spin channels, and a Kohn-Sham gap of ∼0.64 eV at the Fermi level. The major (minor) spin channel is colored blue (red).

layering of the $L2_1$ and $C1_b$ structures along the [111] direction of the underlying cubic lattices (see Fig. 16). We provide the lattice parameters and atomic coordinates of the $Fe_{1.5}TiSb$ phase in Ref. [22].

We calculated the density of electronic states in the ground state $R3m$ structure and find that it is a nonmagnetic semiconductor with a Kohn-Sham gap of ∼0.64 eV (see Fig. 17). We observe that gaps open in both the spin channels and the Fermi energy is in the gap. As discussed in Sec. II, the full-Heusler Fe_2TiSb compound is a Slater-Pauling near half-metal with 25 electrons, a moment of ∼1 Bohr magneton per formula unit (μ_B/f.u.), and a gap in the *minority* spin channel (see Fig. 1). The half-Heusler FeTiSb compound is also a Slater-Pauling near half-metal with 17 electrons, a moment of ∼1 μ_B/f.u. but with a gap in the *majority* spin channel (see Fig. 2). When the full-Heusler and the half-Heusler are layered to form the $Fe_{1.5}TiSb$ compound, there are three electrons per atom in each spin channel, and therefore a Slater-Pauling gap can exist in *both* spin channels. This gap in both spin channels is precisely what we observe in the $Fe_{1.5}TiSb$ compound (see Fig. 17), consistent with Slater-Pauling behavior of these compounds. And this opening of gaps in both spin channels seems to contribute to the stability of the $R3m$ structure. Thus, in full agreement with experimental data, our calculations demonstrate the existence of a $Fe_{1.5}TiSb$ phase, that is, (a) stable relative to Fe_2TiSb and FeTiSb, (b) an ordered Fe/□ arrangement based on the Heusler structure, and (c) is a nonmagnetic semiconductor. The details of the cluster expansion, structural motifs in the predicted low-energy phase, and features of the electronic structure will be discussed in a future publication.

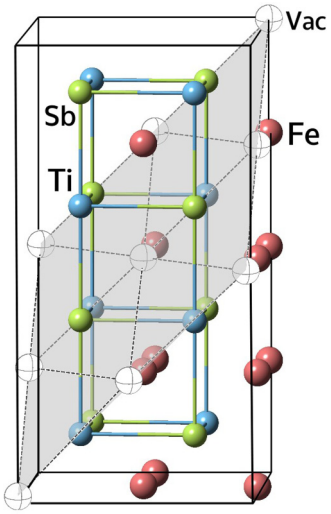

FIG. 16. Structure of the low energy $R3m$ $Fe_{1.5}TiSb$ phase obtained from a cluster expansion illustrating the layering of the $L2_1$ Fe_2TiSb and $C1_b$ FeTiSb along the [111] direction of the underlying cubic lattices. A (111) "defect planes" formed by vacancies is highlighted. Only a part of the periodic cell is shown here for clarity. (Sb = green, Ti = blue, Fe = red, and vacancies = unfilled spheres.)

VI. DISCUSSION AND CONCLUSIONS

We investigated the structural and magnetic properties of the Fe_xTiSb material system, including the half-Heusler FeTiSb ($x = 1$) and the full-Heusler Fe_2TiSb ($x = 2$) compositions as well as the intermediate $Fe_{1.5}TiSb$ composition. In all cases, after heat treatment a dominant $Fe_{1.5}TiSb$ phase was revealed. Heat treatment of as-cast Fe_2TiSb results in $Fe_{1.5}TiSb$ grains with approximately 10% by volume of an Fe-rich precipitate. The Fe-rich precipitate is the main contributor to the magnetic behavior, with the $Fe_{1.5}TiSb$ phase appearing to be weakly paramagnetic. Heat treatment of as-cast FeTiSb also results in the dominant $Fe_{1.5}TiSb$ phase, but with a Ti-Sb-rich precipitate of nominal composition $Sb_{1.8}Ti_{1.5}Fe$. The cluster expansion results show that the FeTiSb half-Heusler is unstable with respect to two-phase decomposition into $Fe_{1.5}TiSb$ and an Fe-deficient phase, $Fe_{0.5}TiSb$. We note that

this Fe-deficient composition is similar to the $Sb_{1.8}Ti_{1.5}Fe$ phase found experimentally. Future experiments are needed to clarify the structure and properties of this phase. Direct synthesis of $Fe_{1.5}TiSb$ resulted in a single phase material with only ∼1.5% precipitates, in accordance with our initial findings and suggesting that it is the dominant phase within the entire metallurgical system. Directly synthesized $Fe_{1.5}TiSb$ was also observed to be weakly paramagnetic. The crystal structure of the $Fe_{1.5}TiSb$ material is related to the cubic $L2_1$ structure, with Fe in the *8c* Wyckoff position and Ti and Sb in *4a* and *4b* positions, respectively. The main difference in contrast to the postulated full Heusler compound is the overall composition of $Fe_{1.5}TiSb$, from which we conclude that in the 16 atom $L2_1$ fcc cell there should be two Fe vacancies.

Our cluster expansion calculations revealed that $Fe_{1.5}TiSb$ is a stable ground-state composition in the Fe_xTiSb system, and is expected to be a nonmagnetic Slater-Pauling semiconductor. We predict the stable, zero-temperature low-energy phase to have a new, interesting structure type, with Fe/□ ordering on the *8c* Wyckoff sites, occurring in the *R*3*m* space group. The special stability of this structure appears to come from the formation of a gap at the Fermi energy for both spin channels, a mechanism which should apply to other Heusler systems. While experimental studies are as yet unable to draw unambiguous conclusions about the positions of the Fe vacancies to confirm the predicted *R*3*m* structure, the observed $Fe_{1.5}TiSb$ composition coupled with the nonmagnetic behavior is consistent with the hypothesized layered structure. From the XRD data, peaks which would distinguish between a defective $L2_1$ structure and an *R*3*m* structure are predicted to be of low intensity, making unambiguous identification of the *R*3*m* structure difficult. While the *R*3*m* structure is predicted to be the lowest energy phase, it is also possible that kinetics on the experimental time scale are insufficient to obtain a fully ordered *R*3*m* structure, and the structure experimentally observed may be a disordered state somewhere between an *R*3*m* and a defective $L2_1$ structure. Further theoretical studies evaluating the free energy and configurational contribution to the entropy would help clarify the situation, as would more detailed structural characterization combined with extended heat treatment.

Concerning the nonmagnetic ground state, recall that Fe_2TiSb has a predicted Slater-Pauling state with a moment of $+1\,\mu_B$ per formula unit, while FeTiSb has a predicted Slater-Pauling state with a moment of $-1\,\mu_B$ per formula unit. The $Fe_{1.5}TiSb$ material has zero moment—in fact there is no moment on any atom in the calculated phases—a bit peculiar for Fe. Locally, however, there will be fluctuations in the concentrations of the Fe vacancies, and with these will be fluctuations in the local magnetic moments. We speculate that at finite temperature, these moments are likely to average to zero, but may also be partly responsible for the upturn in magnetization at low temperature. Further theoretical work on disordered structures would help clarify the magnetic state.

ACKNOWLEDGMENTS

This study was financially supported by NSF DMREF Grant No. 1235396. V.I.H. and C.W. acknowledge support from NSF grant DMR-1309957. This work utilized resources owned and maintained by the Central Analytical Facility, which is supported by The University of Alabama. The computational work was done using Quest High Performance Computing Cluster at Northwestern University, and resources of the National Energy Research Scientific Computing (NERSC) Center, a DOE Office of Science User Facility supported by the Office of Science of the U.S. Department of Energy under Contract No. DE-AC02-05CH11231.

APPENDIX A: METHODOLOGY: DFT CALCULATIONS

All DFT [23] calculations reported in this work were performed using the Vienna *ab initio* simulation package (VASP) [24,25], with projector augmented wave (PAW) [26,27] potentials, and the Perdew-Burke-Ernzerhof (PBE) [28,29] formulation of a generalized gradient approximation (GGA) to the exchange-correlation energy functional. We use a constant energy cutoff of 520 eV for the plane-wave basis set, and Γ-centered *k*-point meshes with a density of ∼8000*k* points per reciprocal atom (KPPRA). All structures were completely relaxed with respect to cell vectors and cell-internal degrees of freedom by minimizing the energy until forces on all atoms were less than 0.1 eV/nm and stresses on the cell were within a few kbar. Fe and Ti atoms were given an initial magnetic moment of $5\mu_B$/atom in a ferromagnetic spin configuration, and then allowed to relax to electronic self-consistency.

APPENDIX B: METHODOLOGY: CLUSTER EXPANSION

A cluster expansion for a binary alloy A_xB_{1-x} with *N* lattice sites can be viewed as a generalized Ising model in which a property $\mathcal{F}$ for any arbitrary configuration $\{\hat{S}_i\}$ is expressed as a linear combination of basis functions defined as the product of occupation variables of the lattice sites:

$$\mathcal{F}(\{\hat{S}_i\}) = J_0 + \sum_i J_i \hat{S}_i + \frac{1}{2!}\sum_{i\neq j} J_{ij}\hat{S}_i\hat{S}_j + \frac{1}{3!}\sum_{i\neq j\neq k} J_{ijk}\hat{S}_i\hat{S}_j\hat{S}_k + \ldots, \tag{B1}$$

where the configuration $\{\hat{S}_i\}$ is the vector of all occupation variables ($=\{\hat{S}_1,\hat{S}_2,\ldots,\hat{S}_N\}$), and the occupation variables $\hat{S}_i = +1$ or -1, depending on whether the site *i* is occupied by an atom of type A or type B. The expression in Eq. (B1) is essentially exact for any property uniquely determined by the atomic configuration [30–32], if all the terms are included in the series, and by extension should hold for a truncated series, if the cluster expansion is well converged. Further, Eq. (B1) can be rewritten as

$$\mathcal{F}(\{\hat{S}_i\}) = J_0 + \sum_f D_f J_f \overline{\Pi}_f(\{\hat{S}_i\}), \tag{B2}$$

where *f* is a set of lattice sites (called a "cluster"). The sum is defined over all clusters *f* that *are not* equivalent by symmetry of the lattice, while the product average $\overline{\Pi}_f$ is taken over all D_f clusters that *are* equivalent to *f* by symmetry of the lattice. The unknown parameters $\{J_f\}$, called effective cluster interactions (ECI), can then be obtained by fitting them to known values of the property $\mathcal{F}$ for a set of configurations, by the structure inversion method [33–35].

The transferability of the fit to unknown configurations (i.e., those not included in the fit) is measured by a leave-one-out cross-validation (CV) score, defined as

$$\text{CV score} = \left[\frac{1}{n}\sum_{i=1}^{n}\left(\mathcal{F}_i^{\text{direct}} - \mathcal{F}_{(i)}^{\text{CE}}\right)^2\right]^{\frac{1}{2}}, \qquad \text{(B3)}$$

where the $\mathcal{F}_{(i)}^{CE}$ are predicted by a least-squares fit to $(n-1)$ directly calculated values of the property, excluding $\mathcal{F}_i^{\text{direct}}$. The set of clusters and ECI that minimizes the CV score is termed the optimum cluster expansion. The usefulness of the cluster expansion approach relies on the ECI being rapidly decreasing functions of the number of sites and intersite separation, so that only a few clusters can be included in Eq. (B2) without a significant loss in accuracy. The cluster expansion reported in this work was constructed using the implementation in the `maps` utility of the Alloy Theoretic Automated Toolkit (ATAT) [22,35,36].

[1] T. Graf and C. Felser, in *Spintronics: From Materials to Devices*, edited by C. Felser and G. H. Fecher (Springer, Dordrecht, 2013).

[2] C. Felser, G. H. Fecher, and B. Balke, Angew. Chem. Int. Ed. **46**, 668 (2007).

[3] B. Balke, S. Wurmehl, G. H. Fecher, C. Felser, and J. Kübler, Sci. Technol. Adv. Mater. **9**, 014102 (2008).

[4] D. Serrate, J. De Teresa, and M. Ibarra, J. Phys. Condens. Matter **19**, 023201 (2007).

[5] H. Kandpal, V. Ksenofontov, M. Wojcik, R. Seshadri, and C. Felser, J. Phys. D: Appl. Phys. **40**, 1587 (2007).

[6] J. E. Saal, S. Kirklin, M. Aykol, B. Meredig, and C. Wolverton, J. Miner. Metals. Mater. Soc. **65**, 1501 (2013).

[7] S. Kirklin, J. E. Saal, B. Meredig, A. Thompson, J. W. Doak, M. Aykol, S. Ruhl, and C. Wolverton (unpublished).

[8] W. H. Butler, A. Ghosh, K. Munira, Tim Lovorn, J. Romero, C. Lample, L. Wilson, J. Ma, Y. Xie, S. Keshavarz, and D. Mildebrath, Heusler Database, http://heusleralloys.mint.ua.edu.

[9] I. Galanaki, Ph. Mavropoulos, and P. H. Dederichs, J. Phys. D: Appl. Phys. **39**, 765 (2006).

[10] I. Galanakis, E. Şaşıoğlu, and K. Özdoğan, Phys. Rev. B **77**, 214417 (2008).

[11] S. Skaftouros, K. Özdoğan, E. Şaşıoğlu, and I. Galanakis, Phys. Rev. B **87**, 024420 (2013).

[12] J. C. Slater, J. Appl. Phys. **8**, 385 (1937).

[13] L. Pauling, Phys. Rev. **54**, 899 (1938).

[14] R. M. Bozorth, Phys. Rev. **79**, 887 (1950).

[15] P. Brown, A. Fox, E. Maslen, M. O'Keefe, and B. Willis, in *International Tables for Crystallography Volume C: Mathematical, Physical and Chemical tables*, edited by E. Prince (Kluwer, Dordrecht, 2006), Chap. 6.1, pp. 554–595.

[16] U. Arndt, D. Creagh, R. Deslattes, J. Hubbell, P. Indelicato, E. Kessler, Jr., and E. Lindroth, in *International Tables for Crystallography Volume C: Mathematical, Physical and Chemical tables*, edited by E. Prince (Kluwer, Dordrecht, 2006), Chap. 4.2, pp. 191–258.

[17] J. Rodriguez-Carvajal, Physica B **192**, 55 (1993).

[18] P. J. Webster, J. Phys. Chem. Solids **32**, 1221 (1971).

[19] K. R. A. Ziebeck and P. J. Webster, J. Phys. Chem. Solids **35**, 1 (1974).

[20] Y. Takamura, R. Nakane, and S. Sugahara, J. Appl. Phys. **105**, 07B109 (2009).

[21] G. L. W. Hart and R. W. Forcade, Phys. Rev. B **77**, 224115 (2008).

[22] See Supplemental Material at http://link.aps.org/supplemental/10.1103/PhysRevB.93.104424 for additional crystal structural information.

[23] W. Kohn, A. Becke, and R. Parr, J. Phys. Chem. **100**, 12974 (1996).

[24] G. Kresse and J. Hafner, Phys. Rev. B **47**, 558 (1993).

[25] G. Kresse and J. Furthmüller, Phys. Rev. B **54**, 11169 (1996).

[26] P. E. Blöchl, Phys. Rev. B **50**, 17953 (1994).

[27] G. Kresse and D. Joubert, Phys. Rev. B **59**, 1758 (1999).

[28] J. P. Perdew, K. Burke, and M. Ernzerhof, Phys. Rev. Lett. **77**, 3865 (1996).

[29] Y. Wang and J. P. Perdew, Phys. Rev. B **44**, 13298 (1991)

[30] J. M. Sanchez, F. Ducastelle, and D. Gratias, Physica A **128**, 334 (1984).

[31] M. Asta, C. Wolverton, D. de Fontaine, and H. Dreyssé, Phys. Rev. B **44**, 4907 (1991).

[32] C. Wolverton, M. Asta, H. Dreyssé, and D. de Fontaine, Phys. Rev. B **44**, 4914 (1991).

[33] J. W. D. Connolly and A. R. Williams, Phys. Rev. B **27**, 5169 (1983).

[34] A. Zunger, in *Statics and Dynamics of Alloy Phase Transformations*, edited by P. E. A. Turchi and A. Gonis, NATO ASI Series (Springer US, New York, 1994).

[35] A. van de Walle, M. Asta, and G. Ceder, Calphad **26**, 539 (2002).

[36] A. van de Walle and G. Ceder, J. Phase Equilib. **23**, 348 (2002).